

Neural Video Depth Stabilizer

Yiran Wang¹ Min Shi¹ Jiaqi Li¹ Zihao Huang¹

Zhiguo Cao¹ Jianming Zhang² Ke Xian^{3*} Guosheng Lin³

¹School of Artificial Intelligence and Automation, Huazhong University of Science and Technology

²Adobe Research ³S-Lab, Nanyang Technological University

{wangyiran,min.shi,lijiaqi_mail,zihaohuang,zgcao}@hust.edu.cn

jianmzha@adobe.com, {ke.xian,gslin}@ntu.edu.sg

<https://github.com/RaymondWang987/NVDS>

Abstract

Video depth estimation aims to infer temporally consistent depth. Some methods achieve temporal consistency by finetuning a single-image depth model during test time using geometry and re-projection constraints, which is inefficient and not robust. An alternative approach is to learn how to enforce temporal consistency from data, but this requires well-designed models and sufficient video depth data. To address these challenges, we propose a plug-and-play framework called *Neural Video Depth Stabilizer (NVDS)* that stabilizes inconsistent depth estimations and can be applied to different single-image depth models without extra effort. We also introduce a large-scale dataset, *Video Depth in the Wild (VDW)*, which consists of 14,203 videos with over two million frames, making it the largest natural-scene video depth dataset to our knowledge. We evaluate our method on the VDW dataset as well as two public benchmarks and demonstrate significant improvements in consistency, accuracy, and efficiency compared to previous approaches. Our work serves as a solid baseline and provides a data foundation for learning-based video depth models. We will release our dataset and code for future research.

1. Introduction

Monocular video depth estimation is a prerequisite for various video applications, *e.g.*, bokeh rendering [26, 48], 2D-to-3D video conversion [14], and object insertion [49]. An ideal video depth model should output depth results with both spatial accuracy and temporal consistency. Although the spatial accuracy has been greatly improved by recent advances in single-image depth models [2, 18, 29, 30, 46] and datasets [15, 19, 42, 43], how to obtain temporal consistency, *i.e.*, removing flickers in the predicted depth se-

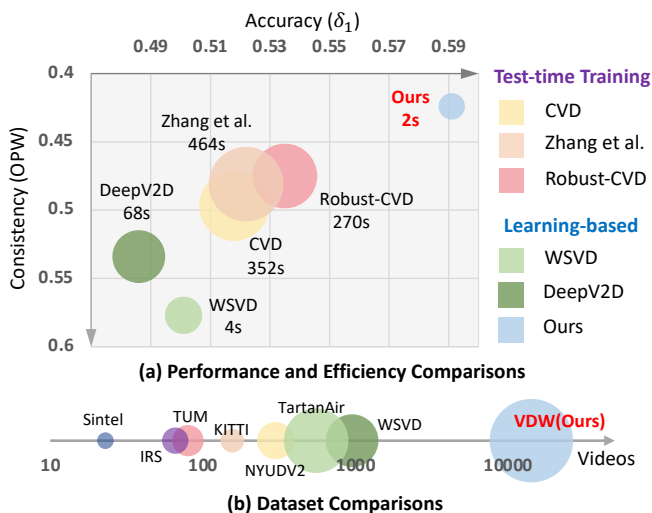


Figure 1: **(a) Performance and efficiency comparisons.** Circle area represents inference time. Smaller circles mean faster speed. The X-axis represents δ_1 on Sintel [6] dataset for spatial accuracy. The Y-axis represents consistent metric *OPW*. Lower *OPW* means better temporal consistency. Our framework outperforms prior arts by large margins. **(b) Dataset comparisons.** Larger circles mean larger amounts of frames. We present VDW dataset, the largest video depth dataset in the wild with diverse scenes.

quences, is still an open question. The prevailing video depth approaches [16, 24, 49] require test-time training (TTT). During inference, a single-image depth model is finetuned on the testing video with geometry constraints and pose estimation. These TTT-based methods have two main issues: limited robustness and heavy computation overhead. Due to the heavy reliance on camera poses, *e.g.*, CVD [24] shows erroneous predictions and robust-CVD [16] produces obvious artifacts for many videos when camera poses [16, 31] are inaccurate. Moreover, test-time

*Corresponding author.

training is extremely time-consuming. CVD [24] takes 40 minutes for 244 frames on four NVIDIA Tesla M40 GPUs.

This motivates us to build a learning-based model that learns to enforce temporal consistency from video depth data. However, like all the deep-learning models, learning-based paradigm requires proper model design and sufficient training data. Previous learning-based methods [7, 36, 41, 47] show worse performance than the TTT-based ones. Video depth data is also limited in scale and diversity.

To address the two aforementioned challenges, we first propose a flexible learning-based framework termed Neural Video Depth Stabilizer (NVDS), which can be directly applied to different single-image depth models. NVDS contains a depth predictor and a stabilization network. The depth predictor can be any off-the-shelf single-image depth model. Different from the previous learning-based methods [7, 36, 41, 47] that function as stand-alone models, NVDS is a plug-and-play refiner for different depth predictors. Specifically, the stabilization network processes initial flickering disparity estimated by the depth predictor and outputs temporally consistent results. Therefore, our framework can benefit from the cutting-edge depth models without extra effort. As for the design of stabilization network, inspired by attention [37] in other video tasks [1, 17, 23, 35], we adopt a cross-attention module in our framework. Each frame can attend relevant information from adjacent frames for temporal consistency. We also design a bidirectional inference strategy to further improve the consistency. As shown in Fig. 1(a), our NVDS outperforms the previous approaches in terms of consistency, accuracy, and efficiency significantly.

Moreover, we collect a large-scale natural-scene video depth dataset, Video Depth in the Wild (VDW), to support the training of robust learning-based models. Current video depth datasets are mostly closed-domain [9, 11, 33, 34, 39]. A few in-the-wild datasets [6, 38, 40] are still limited in quantity, diversity, and quality, *e.g.*, Sintel [6] only contains 23 animated videos. In contrast, our VDW dataset contains 14,203 stereo videos of over 200 hours and 2.23M frames from four different data sources, including movies, animations, documentaries, and web videos. We adopt a rigorous data annotation pipeline to obtain high-quality disparity ground truth for these data. As shown in Fig. 1(b), to the best of our knowledge, VDW is the largest in-the-wild video depth dataset with diverse scenes.

We conduct evaluations on the VDW and two public benchmarks: Sintel [6] and NYUDV2 [33]. Our method achieves state-of-the-art in both the accuracy and the consistency. We also fit three different depth predictors [29, 30, 46] into our framework and evaluate them on NYUDV2 [33]. The results demonstrate the flexibility and effectiveness of our plug-and-play manner. Our main contributions can be summarized as follows:

- We propose a plug-and-play and bidirectional learning-based framework termed Neural Video Depth Stabilizer (NVDS), which can be directly adapted to different single-image depth predictors to remove flickers.
- We propose VDW dataset, which is currently the largest video depth dataset in the wild with the most diverse video scenes.

2. Related Work

Consistent Video Depth Estimation. In addition to predicting spatial-accurate depth, the core task of consistent video depth estimation is to achieve temporal consistency, *i.e.*, removing the flickering effects between consecutive frames. Current video depth estimation approaches can be categorized into test-time training (TTT) ones and learning-based ones. TTT-based methods train an off-the-shelf single-image depth estimation model on testing videos during inference with geometry [16, 24, 49] and pose [16, 31, 32] constraints. The test-time training can be time-consuming. For example, as illustrated by CVD [24], their method takes 40 minutes on 4 NVIDIA Tesla M40 GPUs to process a video of 244 frames. Besides, TTT-based approaches are not robust on in-the-wild videos as they heavily rely on camera poses, which are not reliable for natural scenes. In contrast, the learning-based approaches train video depth models on video depth datasets by spatial and temporal supervision. ST-CLSTM [47] adopts long short-term memory (LSTM) to model temporal relations. FMNet [41] restores the depth of masked frames by the unmasked ones with convolutional self-attention [23]. Cao *et al.* adopt a spatial-temporal propagation network trained by knowledge distillation [12, 22]. However, those methods are independent and cannot refine the results from single-image depth models for consistency. Their performance on consistency and accuracy is also limited. For example, as shown by [41], ST-CLSTM [17] only exploits subsequences of several frames and produces obvious flickers in the outputs. In this paper, we propose a novel framework called Neural Video Depth Stabilizer (NVDS), which can be directly adapted to any off-the-shelf single-image depth models in a plug-and-play manner.

Video Depth Datasets According to the scenes of samples, existing video depth datasets can be categorized into closed-domain datasets and natural-scene datasets. Closed-domain datasets only contain samples in certain scenes, *e.g.*, indoor scenes [9, 33, 39], office scenes [34], and autonomous driving [11]. To enhance the diversity of samples, natural-scene datasets are proposed, which use computer-rendered videos [6, 40] or crawl stereoscopic videos from YouTube [38]. However, the scene diversity and scale of these datasets are still very limited for training robust video depth estimation models that can predict consistent depth in

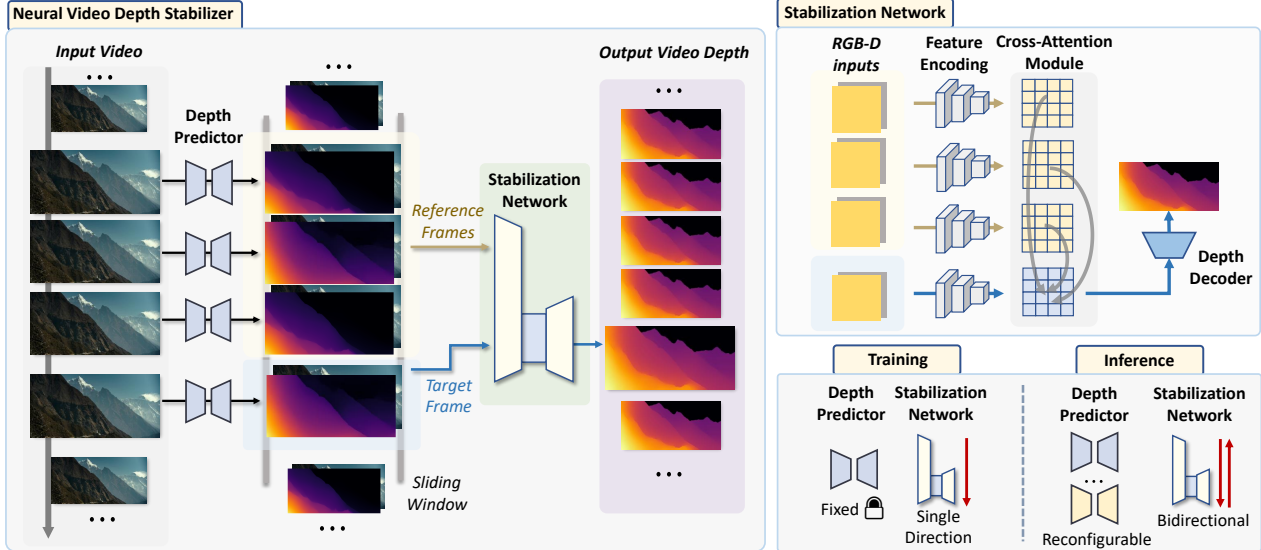


Figure 2: **Overview of the neural video depth stabilizer.** Our framework consists of a depth predictor and a stabilization network. The depth predictor can be any single-image depth model which produces initial flickering disparity maps. Then, the stabilization network refines the flickering disparity maps into temporally consistent ones. The stabilization network functions in a sliding window manner: the frame to be predicted fetches information from adjacent frames for stabilization. During inference, our NVDS framework can be directly adapted to any off-the-shelf depth predictors in a plug-and-play manner. We also devise bidirectional inference to further improve consistency.

the wild. For instance, WSVD [38], which shares a few similar data annotation steps with the proposed VDW dataset, only contains 533 YouTube videos with varied quality and insufficient diversity. Sintel [6] only contains 23 animated videos. To better train and benchmark video depth models, we propose our VDW dataset with 14203 videos from 4 different data sources. To the best of our knowledge, our VDW dataset is currently the largest video depth dataset in the wild with the most diverse scenes.

3. Neural Video Depth Stabilizer

As shown in Fig. 2, the proposed Neural Video Depth Stabilizer (NVDS) consists of a depth predictor and a stabilization network. The depth predictor predicts the initial flickering disparity for each frame. The stabilization network converts the disparity maps into temporally consistent ones. Our NVDS framework can coordinate with any off-the-shelf single-image depth models as depth predictors. We also devise a bidirectional inference strategy to further enhance the temporal consistency during testing.

3.1. Stabilization Network

The stabilization network takes RGB frames along with initial disparity maps as inputs. A backbone [44] encodes the input sequences into depth-aware features. The next step is to build inter-frame correlations. We use a cross-attention module to refine the depth-aware features with temporal in-

formation from relevant frames. Finally, the refined features are fed into a decoder which restores disparity maps with temporal consistency.

Depth-aware Feature Encoding. Stabilization network works in a sliding-window manner: each frame refers to a few previous frames, which are denoted as reference frames, to stabilize the depth. We denote the frame to be predicted as the target frame. Each sliding window consists of four frames.

Due to the varied scale and shift of disparity maps produced by different depth predictors, the initial disparity maps within a sliding window $\mathbf{F} = \{F_1, F_2, F_3, F_4\}$ should be normalized into F_i^{norm} :

$$F_i^{norm} = \frac{F_i - \min(\mathbf{F})}{\max(\mathbf{F}) - \min(\mathbf{F})}, i \in \{1, 2, 3, 4\}. \quad (1)$$

Then, the normalized disparity maps are concatenated with the RGB frames to form a RGB-D sequence. We use a transformer backbone [44] to encode the RGB-D sequence into depth-aware feature maps.

Cross-attention Module. With the depth-aware features, the subsequent phase entails the establishment of inter-frame correlations. We leverage a cross-attention module to build temporal and spatial dependencies across pertinent video frames. Specifically, in the cross-attention module, the target frame selectively attends the relevant features in the reference frames to facilitate depth stabilization. Pixels in the target frame feature maps serve as the query in the

cross-attention operation [37], while the keys and values are generated from the reference frames.

Computational cost can become prohibitively high when employing cross-attention for each position in depth-aware features. Hence, we utilize a patch merging strategy [10] to down-sample the target feature map. Besides, we also restrict the cross-attention into a local window, whereby each token in the target features can only attend a local window in the reference frames. Let T denote the depth-aware feature of the target frame, while R_1, R_2 and R_3 represent the features for the three reference frames. T is partitioned into 7×7 patches with no overlaps; each patch is merged into one token $\mathbf{t} \in \mathbb{R}^c$, where c is the dimension. For each \mathbf{t} , we conduct a local window pooling on R_1, R_2 , and R_3 and stack the pooling results into $R_p \in \mathbb{R}^{c \times 3}$. Then, the cross-attention is computed as:

$$\mathbf{t}' = \text{softmax} \frac{W_q \mathbf{t} (W_k R_p)^T}{\sqrt{c}} W_v R_p, \quad (2)$$

where W_q, W_k , and W_v are learnable linear projections. The cross-attention layer is incorporated into a standard transformer block [37] with residual connection and multi-layer perceptron (MLP). We denote the resulting target feature map refined by the cross-attention module as T_{tem} .

Ultimately, a depth decoder with feature fusion modules [20, 21] integrates the depth-aware feature of the target frame (T) with the cross-attention refined feature T_{tem} , and predicts the consistent disparity map for target frame.

3.2. Training the Stabilization Network

In the training phase, only the stabilization network is optimized. The depth predictor is the freezed pre-trained DPT-L [29]. For the stabilization network, we apply spatial and temporal loss that supervises the depth accuracy and temporal consistency respectively. The training loss can be formulated by:

$$\mathcal{L} = \mathcal{L}_s(n-1) + \mathcal{L}_s(n) + \lambda \mathcal{L}_t(n, n-1), \quad (3)$$

where $\mathcal{L}_s(n-1)$ and $\mathcal{L}_s(n)$ denote the spatial loss of frame $n-1$ and n respectively. $\mathcal{L}_t(n, n-1)$ denotes the temporal loss between frame $n-1$ and n .

We adopt the widely-used affinity invariant loss and gradient matching loss [29, 30] as the spatial loss \mathcal{L}_s . As for the temporal loss, we adopt the optical flow based warping loss [7, 41] to supervise temporal consistency:

$$\mathcal{L}_t(n, n-1) = \frac{1}{M} \sum_{j=1}^M O_{n \Rightarrow n-1}^{(j)} \|D_n^{(j)} - \hat{D}_{n-1}^{(j)}\|_1, \quad (4)$$

where \hat{D}_{n-1} is the predicted disparity D_{n-1} warped by the optical flow $FL_{n \Rightarrow n-1}$. In our implementation, we adopt the GMFlow [45] for optical flow. $O_{n \Rightarrow n-1}$ is the mask calculated as [7, 41] and M denotes pixel numbers. See supplementary for more details on loss functions.

3.3. Bidirectional Inference

Expanding the temporal receptive range can be beneficial for consistency, *e.g.*, adding more former or latter reference frames. However, directly training the stabilization network with bidirectional reference frames will introduce large training burdens. To remedy this, we only train the stabilization network with the former three reference frames. To further enlarge the temporal receptive field and enhance consistency, we introduce a bidirectional inference strategy.

Unlike the training phase, during inference, both the former and latter frames will be used as the reference frames. An additional sliding window is added, where the reference frames are the subsequent three frames of the target. Let us define the stabilizing process as a function $\mathcal{S}(V_t, V_r)$, where V_t and V_r denotes the target RGB-D frame and the reference frames set. When denoting the RGB-D sequence as $\{V_j | j \in 1, 2, \dots, N\}$, N represents frame numbers of a certain video, using this additional sliding window for stabilization can be formulated as:

$$D_n^{post} = \mathcal{S}(V_n, \{V_{n+1}, V_{n+2}, V_{n+3}\}), \quad (5)$$

where V_n denotes the target frame. Likewise, using the original sliding window for stabilization can be denoted by:

$$D_n^{pre} = \mathcal{S}(V_n, \{V_{n-1}, V_{n-2}, V_{n-3}\}). \quad (6)$$

We ensemble the bidirectional results for a larger temporal receptive field as:

$$D_n^{bi} = \frac{(D_n^{pre} + D_n^{post})}{2}. \quad (7)$$

D_n^{bi} denotes the final disparity prediction of the n^{th} frame (target frame). This bidirectional manner can further improve the temporal consistency as demonstrated in Sec. 5.4.

Note that, the cross-attention module is shared by the two sliding windows for inference. Besides, the initial disparity maps and depth-aware features are pre-computed. Hence, the bidirectional inference only increases the inference time by 30% compared with single-direction inference and brings no extra computation for the training process.

In addition to bidirectional inference, the depth predictor can be reconfigurable during inference. For example, simply using a more advanced model NeWCRFs [46] as the depth predictor can obtain performance gain without extra training, as shown in Table 5. As the depth accuracy can be inherited from state-of-the-art depth predictor, our neural video depth stabilizer (NVDS) framework can focus on the learning of depth stabilization and combine the depth accuracy with temporal consistency.

3.4. Implementation Details

Model Architecture. We use the DPT-L [29], Midas-v2 [30], and NeWCRFs [46] as the single-image depth predictors during inference, while only the disparity maps from

| Type | Dataset | Videos | Frames(k) | Indoor | Outdoor | Dynamic | Resolution |
|----------------|----------------|--------|---------------|--------|---------|---------|------------|
| Closed Domains | NYUDV2 [33] | 464 | 407 | ✓ | ✗ | ✗ | 640 × 480 |
| | KITTI [11] | 156 | 94 | ✗ | ✓ | ✓ | 1224 × 370 |
| | TUM [34] | 80 | 128 | ✓ | ✗ | ✓ | 640 × 480 |
| | IRS [39] | 76 | 103 | ✓ | ✗ | ✗ | 960 × 540 |
| | ScanNet [9] | 1,513 | 2,500 | ✓ | ✗ | ✗ | 640 × 480 |
| Natural Scenes | Sintel [6] | 23 | 1 | ✓ | ✓ | ✓ | 1024 × 436 |
| | TartanAir [40] | 1,037 | 1,000 | ✓ | ✓ | ✗ | 640 × 480 |
| | WSVD [38] | 553 | 1,500 | ✓ | ✓ | ✓ | ~ 720p |
| | Ours | 14,203 | 2,237 | ✓ | ✓ | ✓ | 1880 × 800 |

Table 1: **Comparisons of different video depth datasets.** The proposed VDW dataset shows advantages in diversity and quantity.

DPT-L are used during training. Midas-v2 [30] is the same depth model as TTT-based methods [16, 24, 49] for fair comparisons. Mit-b5 [44] is adopted as the backbone to encode depth-aware features. For each target frame, we use three reference frames with inter-frame intervals $l = 1$.

Training Recipe. All frames are resized so that the shorter side equals 384, and then randomly cropped to 384×384 for training. In each epoch, we randomly sample 72,000 input sequences. Note that the sampled frames in each epoch does not overlap. We use Adam optimizer to train the model for 30 epochs with a batchsize of 9. The initial learning rate is set to $6e - 5$ and decreases by $1e - 5$ for every five epochs. When finetuning our model on NYUDV2 [33], we use a learning rate of $1e - 5$ for only one epoch. In all experiments, the temporal loss weight λ is set to 0.2.

4. VDW Dataset

As mentioned in Sec. 1, current video depth datasets are limited in both diversity and volume. To compensate for the data shortage and boost the performance of learning-based video depth models, we elaborate a large-scale natural-scene dataset, Video Depth in the Wild (VDW). To our best knowledge, our VDW dataset is currently the largest video depth dataset with the most diverse video scenes.

Dataset Construction. We collect stereo videos from four data sources: movies, animations, documentaries, and web videos. A total of 60 movies, animations, and documentaries in Blu-ray format are collected. We also crawl 739 web stereo videos from YouTube with the keywords such as “stereoscopic” and “stereo”. To balance the realism and diversity, only 24 movies, animations, and documentaries are retained. For instance, “Seven Wonders of the Solar System” is removed as it contains many virtual scenes. The disparity ground truth is generated with two main steps: sky segmentation and optical flow estimation. A model ensemble manner is adopted to remove errors and noises in the sky masks, which can improve the quality of the ground truth and the performance of the trained models, especially on sky regions as shown in Fig. 4. A state-of-the-art optical

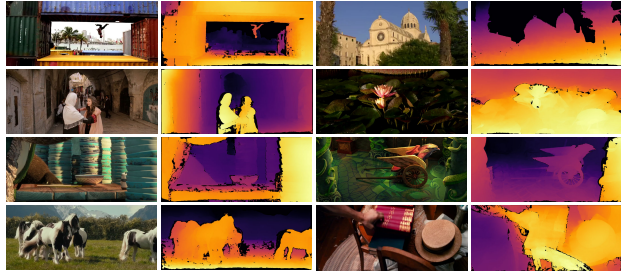


Figure 3: **Examples of our VDW dataset.** Four rows are from web videos, documentaries, animations, and movies, respectively. Sky regions and invalid pixels are masked out.

flow model GMFlow [45] is used to generate the disparity ground truth. Finally, a rigorous data cleaning procedure is conducted to filter the videos that are not qualified for our dataset. Fig. 3 shows some examples of our VDW dataset.

Dataset Statistics. VDW dataset contains 14,203 videos with a total of 2,237,320 frames. The total data collection and processing time takes over six months and about 4,000 man-hours. To verify the diversity of scenes and entities in our dataset, we conduct semantic segmentation by Mask2Former [8] trained on ADE20k [50]. All the 150 categories are covered in our dataset, and each category can be found in at least 50 videos. We randomly choose 104 videos with 13,963 frames as the test set. The testing videos adopt different data sources from the training data, *i.e.*, different movies, web videos, or animations. Our VDW not only alleviates the data shortage for learning-based approaches, but also serves as a comprehensive benchmark for video depth.

Comparisons with Other Datasets. As shown in Table 1, the proposed VDW dataset has significantly larger numbers of video scenes. Compared with the closed-domain datasets [9, 11, 33, 34, 39], the videos of VDW are not restricted to a certain scene, which is more helpful to train a robust video depth model. For the natural-scene datasets, our dataset has more than ten times the number of videos as the previous largest dataset WSVD [38]. Although WSVD [38] has 1.5M frames, the scenes (video numbers) are limited. It is also worth noticing that our VDW dataset has higher resolution and a rigorous data annotation and cleaning pipeline. We only collect videos with resolutions over 1080p and crop all our videos to 1880×800 to remove black bars and subtitles. See supplementary for more statistics and data construction process of the VDW dataset.

5. Experiments

To prove the effectiveness of our framework Neural Video Depth Stabilizer (NVDS), we conduct experiments on 3 different datasets, which contain videos for real-world and synthetic, static and dynamic, indoor and outdoor.

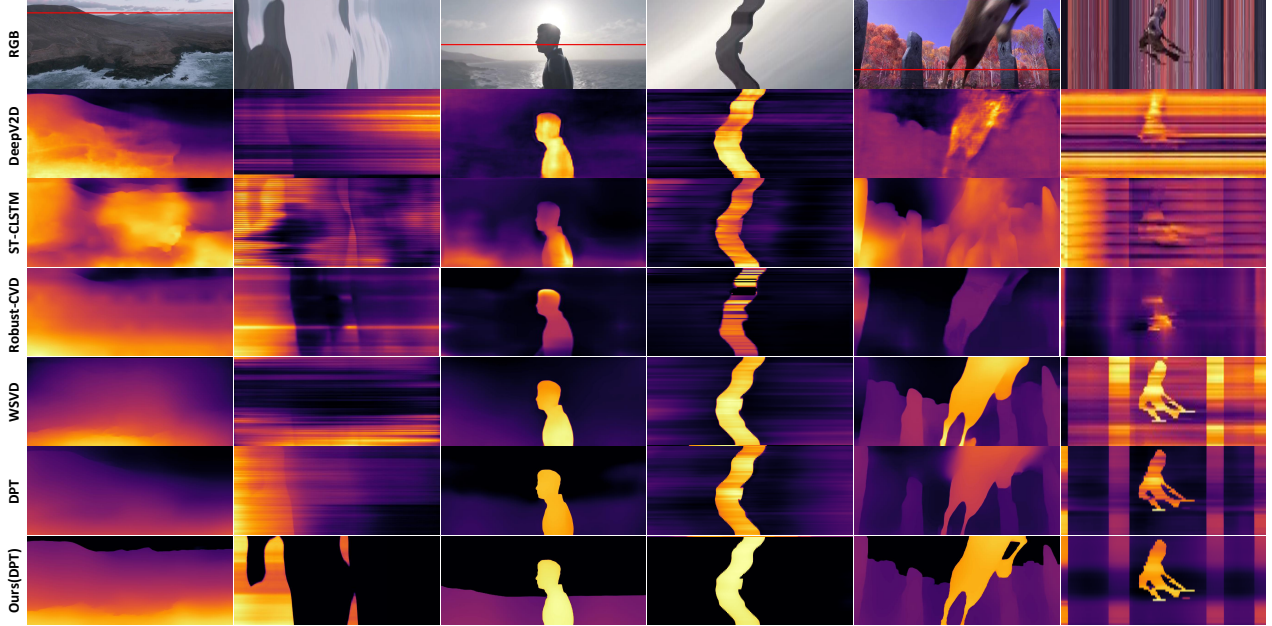


Figure 4: **Qualitative comparisons.** DeepV2D [36] and Robust-CVD [16] show obvious artifacts in those videos. We draw the scanline slice over time; fewer zigzagging pattern means better consistency. Compared with the other video depth methods, our NVDS is more robust on natural scenes and achieves better spatial accuracy and temporal consistency.

5.1. Datasets and Evaluation Protocol

VDW Dataset. We use the proposed VDW as the training data for its diversity and quantity on natural scenes. We also evaluate the previous video depth approaches on the test split of VDW, serving as a new video depth benchmark.

Sintel Dataset. Following [16, 49], we use the final version of Sintel [6] to demonstrate the generalization ability of our NVDS. We conduct zero-shot evaluations on Sintel [6]. All learning-based methods are not finetuned on Sintel dataset.

NYUDV2 Dataset. Except for natural scenes, a closed-domain NYUDV2 [33] is adopted for evaluation. We pre-train the stabilization network on VDW and finetune the model on NYUDV2 [33] dataset. Besides, we also test our NVDS on Davis [27] for qualitative comparisons.

Evaluation Metrics. We evaluate both the depth accuracy and temporal consistency of different methods. For the temporal consistency metric, we adopt the optical flow based warping metric (*OPW*) following FMNet [41], which can be computed as:

$$OPW = \frac{1}{N-1} \sum_{n=2}^N \mathcal{L}^t(n, n-1). \quad (8)$$

We report the average *OPW* of all the videos in the testing sets. As for the depth metrics, we adopt the commonly-applied *Rel* and $\delta_i (i = 1, 2, 3)$.

5.2. Comparisons with Other Video Depth Methods

Comparisons with the TTT-based methods. First focus on the test-time training (TTT) approaches [16, 24, 49]. As shown in Table 2, our learning-based framework outperforms TTT-based approaches by large margins in terms of inference speed, accuracy and consistency. Our NVDS shows at least 6.4% and 7.6% improvements for δ_1 and *OPW* than Robust-CVD [16] on VDW, Sintel [6], and NYUDV2 [33]. Our learning-based approach is over one hundred times faster than Robust-CVD [16]. Our strong performance demonstrates that learning-based frameworks are capable of attaining great performance with much higher efficiency than TTT-based methods [16, 24, 49].

It is also worth-noticing that the TTT-based approaches are not robust for natural scenes. CVD [24] and Zhang *et al.* [49] fail on some videos on VDW and Sintel [6] dataset due to erroneous pose estimation results. Hence, some of their results are not reported in Table 2. Refer to supplementary for more details. Although Robust-CVD [16] can produce results for all testing videos by jointly optimizing the camera poses and depth, it is still not robust for many videos and produces obvious artifacts as shown in Fig. 4.

Comparisons with the learning-based methods. The proposed neural video depth stabilizer also attains better accuracy and consistency than previous learning-based approaches [7, 38, 41, 47] on all the three datasets, including natural scenes and closed domain. As shown in Ta-

| Type | Method | Time(s) | VDW | | | Sintel | | | NYUDV2 | | |
|--------------------|--------------------------|---------|---------------------|------------------|------------------|---------------------|------------------|------------------|---------------------|------------------|------------------|
| | | | $\delta_1 \uparrow$ | Rel \downarrow | OPW \downarrow | $\delta_1 \uparrow$ | Rel \downarrow | OPW \downarrow | $\delta_1 \uparrow$ | Rel \downarrow | OPW \downarrow |
| Single Image | Midas [30] | 0.76 | 0.644 | 0.347 | 0.647 | 0.485 | 0.410 | 0.843 | 0.910 | 0.095 | 0.862 |
| | DPT [29] | 0.97 | <u>0.724</u> | <u>0.266</u> | 0.461 | 0.597 | <u>0.339</u> | 0.612 | 0.928 | 0.084 | 0.811 |
| Test-time Training | CVD [24] | 352.58 | – | – | – | 0.518 | 0.406 | 0.497 | – | – | – |
| | Robust-CVD [16] | 270.28 | 0.658 | 0.334 | 0.251 | 0.521 | 0.422 | 0.475 | 0.886 | 0.103 | 0.394 |
| | Zhang <i>et al.</i> [49] | 464.83 | – | – | – | 0.522 | 0.342 | 0.481 | – | – | – |
| Learning Based | ST-CLSTM [47] | 0.58 | 0.461 | 0.589 | 0.455 | 0.351 | 0.517 | 0.585 | 0.833 | 0.131 | 0.645 |
| | Cao <i>et al.</i> [7] | – | – | – | – | – | – | – | 0.835 | 0.131 | – |
| | FMNet [41] | 3.87 | 0.465 | 0.584 | 0.388 | 0.357 | 0.513 | 0.521 | 0.832 | 0.134 | 0.387 |
| | DeepV2D [36] | 68.71 | 0.522 | 0.628 | 0.425 | 0.486 | 0.526 | 0.534 | 0.924 | 0.082 | 0.402 |
| | WSVD [38] | 4.25 | 0.621 | 0.379 | 0.437 | 0.501 | 0.439 | 0.577 | 0.768 | 0.164 | 0.683 |
| | Ours(Midas) | 1.55 | 0.694 | 0.286 | <u>0.164</u> | 0.532 | 0.374 | <u>0.469</u> | <u>0.941</u> | <u>0.076</u> | <u>0.373</u> |
| | Ours(DPT) | 1.73 | 0.731 | 0.259 | 0.138 | <u>0.591</u> | 0.335 | 0.424 | 0.950 | 0.072 | 0.364 |

Table 2: **Comparisons with the state-of-the-art approaches.** We report the total time of processing eight 640×480 frames by different methods on one NVIDIA RTX A6000 GPU. Best performance is in boldface. Second best is underlined.

| Method | $\delta_1 \uparrow$ | $\delta_2 \uparrow$ | $\delta_3 \uparrow$ | Rel \downarrow | OPW \downarrow |
|-----------------------|---------------------|---------------------|---------------------|------------------|------------------|
| SC-DepthV1 [4] | 0.813 | 0.952 | 0.987 | 0.143 | 0.465 |
| SC-DepthV2 [3] | 0.820 | 0.956 | 0.989 | 0.138 | 0.474 |
| ST-CLSTM [47] | 0.833 | 0.965 | 0.991 | 0.131 | 0.645 |
| Cao <i>et al.</i> [7] | 0.835 | 0.965 | 0.990 | 0.131 | – |
| FMNet [41] | 0.832 | 0.968 | 0.992 | 0.134 | 0.387 |
| DeepV2D [36] | 0.924 | 0.982 | 0.994 | 0.082 | 0.402 |
| Ours-scratch(DPT) | 0.931 | 0.988 | 0.997 | 0.081 | 0.372 |

Table 3: **Comparisons of the learning-based approaches on NYUDV2 [33] dataset.** All the compared methods use NYUDV2 [33] as the training and evaluation data. Our neural video depth stabilizer trained from scratch also achieves better performance than all the other methods.

ble 2, on our VDW and Sintel with natural scenes, the proposed NVDS shows obvious advantages: improving δ_1 and OPW by over 9% and 18.6% compared with previous learning-based methods. Note that, our NVDS can benefit from stronger single-image models and obtain better performance, which will be discussed in Table 5.

To better compare NVDS with previous learning-based method, we only use NYUDV2 [33] as training and evaluation data for comparisons. As shown in Table 3, the proposed NVDS improves the FMNet [41] by 9.9% and 3.8% in terms of δ_1 and OPW. We also achieve better performance than DeepV2D [36], which is the previous state-of-the-art structure-from-motion-based methods but can only deal with completely static scenes. The results demonstrate that using our architecture alone can also obtain better video depth performance.

Qualitative Comparisons. We show some qualitative comparisons on natural-scene videos in Fig. 4. We draw the scanline slice over time. Fewer zigzagging pattern means

| Dataset | $\delta_1 \uparrow$ | OPW \downarrow | Setting | $\delta_1 \uparrow$ | OPW \downarrow |
|---------------|---------------------|------------------|-----------------|---------------------|------------------|
| NYUDV2 | 0.527 | 0.435 | Scratch(DPT) | 0.931 | 0.372 |
| IRS+TartanAir | 0.542 | 0.489 | Pretrain(Midas) | 0.941 | 0.373 |
| VDW(Ours) | 0.591 | 0.424 | Pretrain(DPT) | 0.950 | 0.364 |

(a) Different Training Data

(b) Pretraining and Finetuning

Table 4: **Influence of different training data.** (a) Training with different datasets. We conduct zero-shot evaluations on Sintel [6] with different training data for our NVDS. (b) Pretraining and finetuning. Pretraining on our VDW can further improve the results on the closed-domain NYUDV2 [33], compared with training from scratch.

better consistency. The initial estimation of DPT [29] in the sixth row contains flickers and blurs, which are eliminated with the proposed NVDS, as shown in the last row. Although the TTT-based Robust-CVD [16] shows competitive performances on the indoor NYUDV2 [33] dataset, it is not robust on the natural scenes. As can be observed in the fourth row, Robust-CVD produces obvious artifacts due to erroneous pose estimation.

One can also observe that we produce much sharper estimation at the edges, especially on the skylines, which can be down to our rigorous annotation pipeline for VDW, *e.g.*, the ensemble strategy for sky segmentation.

Influence of Training Data. The quality and diversity of data can greatly influence the learning-based video depth models. Our VDW dataset offers hundreds of times more data and scenes compared to previous works, which can be used to train robust learning-based models in the wild. To better show the difference, we compare our dataset with the existing datasets under zero-shot cross-dataset setting. As shown in Table 4 (a), we train our NVDS with existing video depth datasets [33, 39, 40] and evaluate the model

| | Initial | | | Ours | | |
|--------------|---------------------|-------------------------|-------------------------|---------------------|-------------------------|-------------------------|
| | $\delta_1 \uparrow$ | <i>Rel</i> \downarrow | <i>OPW</i> \downarrow | $\delta_1 \uparrow$ | <i>Rel</i> \downarrow | <i>OPW</i> \downarrow |
| Midas [30] | 0.910 | 0.095 | 0.862 | 0.941 | 0.076 | 0.373 |
| DPT [29] | 0.928 | 0.084 | 0.811 | 0.950 | 0.072 | 0.364 |
| NeWCRFs [46] | 0.937 | 0.072 | 0.645 | 0.957 | 0.068 | 0.326 |

Table 5: **Comparisons of different depth predictors on the NYUDV2 [33] dataset.** Our framework is compatible with different depth predictors in a plug-and-play manner.

| Method | $\delta_1 \uparrow$ | <i>OPW</i> \downarrow | Method | $\delta_1 \uparrow$ | <i>OPW</i> \downarrow |
|---------------|---------------------|-------------------------|---------------|---------------------|-------------------------|
| DPT [29] | 0.724 | 0.461 | Midas [30] | 0.644 | 0.647 |
| Pre-window | 0.730 | 0.159 | Pre-window | 0.694 | 0.175 |
| Post-window | 0.731 | 0.152 | Post-window | 0.694 | 0.182 |
| Bidirectional | 0.731 | 0.138 | Bidirectional | 0.694 | 0.164 |

(a) DPT Initialization

(b) Midas Initialization

Table 6: **Ablation of bidirectional inference on VDW.** Bidirectional inference with larger temporal receptive fields can further improve the consistency.

on Sintel [6] dataset. With both quantity and diversity, using VDW as the training data yields the best accuracy and consistency. Large closed-domain dataset NYUDV2 [33] or synthetic natural-scene dataset like IRS [39] and TartanAir [40] are not sufficient for training in-the-wild video-depth models.

Moreover, although the proposed VDW is designed for natural scenes, it can also boost the performance on closed domains by serving as pretraining data. As in Table 4 (b), the VDW-pretrained model outperforms the model that is trained from scratch, even with weaker single-image model (Midas [30]). This suggests that VDW can also benefit some closed-domain scenarios.

5.3. Inference Speed Comparisons

To evaluate the efficiency, we compare the inference time on a 640×480 video with eight frames. The inference is conducted on one NVIDIA RTX A6000 GPU. As shown in Table 2, the proposed NVDS reduces the inference time by hundreds of times compared to the TTT-based approaches CVD [24], Robust-CVD [16], and Zhang *et al.* [49]. The learning-based method DeepV2D [36] alternately estimates depth and camera poses, which is time-consuming. WSVD [38] is also slow because they need to compute optical flow [13] between consecutive frames while inference.

5.4. Ablation Studies

Here we verify the effectiveness of the proposed method. We first ablate the plug-and-play manner with different single-image depth models. Besides, We also discuss the bidirectional inference, the temporal loss, and the intervals of reference frames.

| Method | $\delta_1 \uparrow$ | <i>OPW</i> \downarrow | Method | $\delta_1 \uparrow$ | <i>OPW</i> \downarrow |
|---------------------|---------------------|-------------------------|---------|---------------------|-------------------------|
| DPT [29] | 0.621 | 0.492 | $l = 1$ | 0.625 | 0.216 |
| $w/o \mathcal{L}^t$ | 0.627 | 0.303 | $l = 3$ | 0.618 | 0.219 |
| w/ \mathcal{L}^t | 0.625 | 0.216 | $l = 5$ | 0.621 | 0.246 |

(a) Temporal Loss

(b) Inter-frame Intervals

Table 7: **Temporal loss and inter-frame intervals l .** We randomly split 100 videos for training and 10 videos for testing from our VDW dataset in these two experiments.

Plug-and-play Manner. As shown in Table 5, we directly adapt our NVDS to three different state-of-the-art single-image depth models DPT [29], Midas [30], and NeWCRFs [46]. By post-processing their initial flickering disparity maps, our NVDS achieves better temporal consistency and spatial accuracy. With higher initial depth accuracy, the spatial performance of our NVDS is also improved. The experiment demonstrates the effectiveness of our plug-and-play manner. To be mentioned, the NeWCRFs [46] is only trained on NYUDV2 [33]. Thus, we only report our results with NeWCRFs [46] on the NYUDV2 [33] dataset.

Bidirectional Inference. As shown in Table 6, whether using DPT [29] or Midas[30] as the single-image depth predictor, our NVDS can already enforce the temporal consistency with previous or post sliding window of target frame. The bidirectional inference can further improve the consistency with larger bidirectional temporal receptive fields.

Temporal Loss. As in Table 7 (a), even without the temporal loss as explicit supervision, our stabilization network can already enforce temporal consistency. Adding the temporal loss can further remove the flickers and improve the temporal consistency.

Reference Frame Intervals. We denote the inter-frame intervals as l . As shown in Table 7 (b), $l = 1$ attains the best performance in our experiments.

6. Conclusion

In this paper, we propose a Neural Video Depth Stabilizer framework and a large-scale natural-scene VDW dataset for video depth estimation. Different from previous learning-based video depth models that function as stand-alone models, our Neural Video Depth Stabilizer learns to stabilize the flickering results from the estimations of single-image depth models. In this way, Neural Video Depth Stabilizer can focus on the learning of temporal consistency, while inheriting the depth accuracy from the cutting-edge depth predictors without further tuning. We also elaborate on the VDW dataset to alleviate the data shortage. To our best knowledge, it is currently the largest video depth dataset in the wild. We hope our work can serve as a solid baseline and provide a data foundation for the

learning-based video depth models.

Limitations and future work. Currently, we only offer one implementation for the NVDS framework. In future work, we will consider using more mechanisms in the stabilization network and adding more implementations for different applications, *e.g.*, the lightweight models.

Acknowledgments. This work was funded by Adobe.

References

- [1] Anurag Arnab, Mostafa Dehghani, Georg Heigold, Chen Sun, Mario Lučić, and Cordelia Schmid. Vivit: A video vision transformer. In *Proceedings of the IEEE/CVF International Conference on Computer Vision (ICCV)*, pages 6836–6846, 2021. [2](#)
- [2] Shariq Farooq Bhat, Ibraheem Alhashim, and Peter Wonka. Adabins: Depth estimation using adaptive bins. In *Proceedings of the IEEE/CVF Conference on Computer Vision and Pattern Recognition (CVPR)*, pages 4009–4018, 2021. [1](#)
- [3] Jia-Wang Bian, Huangying Zhan, Naiyan Wang, Tat-Jun Chin, Chunhua Shen, and Ian Reid. Auto-rectify network for unsupervised indoor depth estimation. *IEEE transactions on pattern analysis and machine intelligence*, 44(12):9802–9813, 2022. [7](#)
- [4] Jia-Wang Bian, Huangying Zhan, Naiyan Wang, Zhichao Li, Le Zhang, Chunhua Shen, Ming-Ming Cheng, and Ian Reid. Unsupervised scale-consistent depth learning from video. *International Journal of Computer Vision (IJCV)*, 2021. [7](#)
- [5] Samuel Rota Bulo, Lorenzo Porzi, and Peter Kotschieder. In-place activated batchnorm for memory-optimized training of dnn. In *Proceedings of the IEEE/CVF Conference on Computer Vision and Pattern Recognition (CVPR)*, pages 5639–5647, 2018. [11](#)
- [6] Daniel J Butler, Jonas Wulff, Garrett B Stanley, and Michael J Black. A naturalistic open source movie for optical flow evaluation. In *European Conference on Computer Vision (ECCV)*, pages 611–625. Springer, 2012. [1](#), [2](#), [3](#), [5](#), [6](#), [7](#), [8](#), [15](#), [17](#)
- [7] Yuanzhouhan Cao, Yidong Li, Haokui Zhang, Chao Ren, and Yifan Liu. Learning structure affinity for video depth estimation. In *Proceedings of the 29th ACM International Conference on Multimedia*, pages 190–198, 2021. [2](#), [4](#), [6](#), [7](#)
- [8] Bowen Cheng, Ishan Misra, Alexander G Schwing, Alexander Kirillov, and Rohit Girdhar. Masked-attention mask transformer for universal image segmentation. In *Proceedings of the IEEE/CVF Conference on Computer Vision and Pattern Recognition (CVPR)*, pages 1290–1299, 2022. [5](#), [11](#), [12](#)
- [9] Angela Dai, Angel X Chang, Manolis Savva, Maciej Halber, Thomas Funkhouser, and Matthias Nießner. Scannet: Richly-annotated 3d reconstructions of indoor scenes. In *Proceedings of the IEEE/CVF Conference on Computer Vision and Pattern Recognition (CVPR)*, pages 5828–5839, 2017. [2](#), [5](#)
- [10] Alexey Dosovitskiy, Lucas Beyer, Alexander Kolesnikov, Dirk Weissenborn, Xiaohua Zhai, Thomas Unterthiner, Mostafa Dehghani, Matthias Minderer, Georg Heigold, Sylvain Gelly, et al. An image is worth 16x16 words: Transformers for image recognition at scale. In *International Conference on Learning Representations*, 2020. [4](#)
- [11] Andreas Geiger, Philip Lenz, Christoph Stiller, and Raquel Urtasun. Vision meets robotics: The kitti dataset. *The International Journal of Robotics Research*, 32(11):1231–1237, 2013. [2](#), [5](#)
- [12] Geoffrey Hinton, Oriol Vinyals, Jeff Dean, et al. Distilling the knowledge in a neural network. *arXiv preprint arXiv:1503.02531*, 2(7), 2015. [2](#)
- [13] Eddy Ilg, Nikolaus Mayer, Tonmoy Saikia, Margret Keuper, Alexey Dosovitskiy, and Thomas Brox. FlowNet 2.0: Evolution of optical flow estimation with deep networks. In *Proceedings of the IEEE/CVF Conference on Computer Vision and Pattern Recognition (CVPR)*, pages 2462–2470, 2017. [8](#)
- [14] Kevin Karsch, Ce Liu, and Sing Bing Kang. Depth transfer: Depth extraction from video using non-parametric sampling. *IEEE transactions on pattern analysis and machine intelligence*, 36(11):2144–2158, 2014. [1](#)
- [15] Youngjung Kim, Hyungjoo Jung, Dongbo Min, and Kwanghoon Sohn. Deep monocular depth estimation via integration of global and local predictions. *IEEE Transactions on Image Processing*, 27(8):4131–4144, 2018. [1](#)
- [16] Johannes Kopf, Xuejian Rong, and Jia-Bin Huang. Robust consistent video depth estimation. In *Proceedings of the IEEE/CVF Conference on Computer Vision and Pattern Recognition (CVPR)*, pages 1611–1621, 2021. [1](#), [2](#), [5](#), [6](#), [7](#), [8](#), [15](#), [17](#)
- [17] Jiangtong Li, Wentao Wang, Junjie Chen, Li Niu, Jianlou Si, Chen Qian, and Liqing Zhang. Video semantic segmentation via sparse temporal transformer. In *Proceedings of the 29th ACM International Conference on Multimedia*, MM ’21, page 59–68, New York, NY, USA, 2021. Association for Computing Machinery. [2](#)
- [18] Ruibo Li, Ke Xian, Chunhua Shen, Zhiguo Cao, Hao Lu, and Lingxiao Hang. Deep attention-based classification network for robust depth prediction. In *Asian Conference on Computer Vision (ACCV)*, pages 663–678, 2018. [1](#)
- [19] Zhengqi Li and Noah Snavely. Megadepth: Learning single-view depth prediction from internet photos. In *Proceedings of the IEEE/CVF Conference on Computer Vision and Pattern Recognition (CVPR)*, June 2018. [1](#)
- [20] Guosheng Lin, Anton Milan, Chunhua Shen, and Ian Reid. Refinenet: Multi-path refinement networks for high-resolution semantic segmentation. In *Proceedings of the IEEE/CVF Conference on Computer Vision and Pattern Recognition (CVPR)*, pages 1925–1934, 2017. [4](#), [11](#), [12](#)
- [21] Tsung-Yi Lin, Piotr Dollár, Ross Girshick, Kaiming He, Bharath Hariharan, and Serge Belongie. Feature pyramid networks for object detection. In *Proceedings of the IEEE/CVF Conference on Computer Vision and Pattern Recognition (CVPR)*, pages 2117–2125, 2017. [4](#), [12](#)
- [22] Yifan Liu, Ke Chen, Chris Liu, Zengchang Qin, Zhenbo Luo, and Jingdong Wang. Structured knowledge distillation for semantic segmentation. In *Proceedings of the IEEE/CVF Conference on Computer Vision and Pattern Recognition (CVPR)*, pages 2604–2613, 2019. [2](#)
- [23] Zhouyong Liu, Shun Luo, Wubin Li, Jingben Lu, Yufan Wu, Shilei Sun, Chunguo Li, and Luxi Yang. Convtransformer: A convolutional transformer network for video frame syn-

- thesis. *arXiv preprint arXiv:2011.10185*, 2020. **2**
- [24] Xuan Luo, Jia-Bin Huang, Richard Szeliski, Kevin Matzen, and Johannes Kopf. Consistent video depth estimation. *ACM Transactions on Graphics (ToG)*, 39(4):71–1, 2020. **1, 2, 5, 6, 7, 8, 15, 17**
- [25] Simon Meister, Junhwa Hur, and Stefan Roth. Unflow: Un-supervised learning of optical flow with a bidirectional census loss. In *Proceedings of the AAAI conference on artificial intelligence*, volume 32, 2018. **11**
- [26] Juewen Peng, Zhiguo Cao, Xianrui Luo, Hao Lu, Ke Xian, and Jianming Zhang. Bokehme: When neural rendering meets classical rendering. In *Proceedings of the IEEE/CVF Conference on Computer Vision and Pattern Recognition (CVPR)*, pages 16283–16292, 2022. **1**
- [27] Jordi Pont-Tuset, Federico Perazzi, Sergi Caelles, Pablo Arbeláez, Alexander Sorkine-Hornung, and Luc Van Gool. The 2017 davis challenge on video object segmentation. *arXiv preprint arXiv:1704.00675*, 2017. **6, 17**
- [28] PySceneDetect developers. PySceneDetect. <http://scenedetect.com>. [Online; Accessed 2022]. **11**
- [29] René Ranftl, Alexey Bochkovskiy, and Vladlen Koltun. Vision transformers for dense prediction. In *Proceedings of the IEEE/CVF International Conference on Computer Vision (ICCV)*, pages 12179–12188, 2021. **1, 2, 4, 7, 8, 12, 13, 15**
- [30] René Ranftl, Katrin Lasinger, David Hafner, Konrad Schindler, and Vladlen Koltun. Towards robust monocular depth estimation: Mixing datasets for zero-shot cross-dataset transfer. *IEEE transactions on pattern analysis and machine intelligence*, 44(03):1623–1637, 2020. **1, 2, 4, 5, 7, 8, 11, 12, 13, 15**
- [31] Johannes Lutz Schönberger and Jan-Michael Frahm. Structure-from-motion revisited. In *Proceedings of the IEEE/CVF Conference on Computer Vision and Pattern Recognition (CVPR)*, pages 4104–4113, 2016. **1, 2**
- [32] Johannes Lutz Schönberger, Enliang Zheng, Marc Pollefeys, and Jan-Michael Frahm. Pixelwise view selection for unstructured multi-view stereo. In *European Conference on Computer Vision (ECCV)*, volume 9907, pages 501–518, 2016. **2**
- [33] Nathan Silberman, Derek Hoiem, Pushmeet Kohli, and Rob Fergus. Indoor segmentation and support inference from rgb-d images. In *European Conference on Computer Vision (ECCV)*, pages 746–760. Springer, 2012. **2, 5, 6, 7, 8, 17**
- [34] Jürgen Sturm, Nikolas Engelhard, Felix Endres, Wolfram Burgard, and Daniel Cremers. A benchmark for the evaluation of rgb-d slam systems. In *IEEE/RSJ International Conference on Intelligent Robots and Systems (IROS)*, pages 573–580. IEEE, 2012. **2, 5**
- [35] Guolei Sun, Yun Liu, Henghui Ding, Thomas Probst, and Luc Van Gool. Coarse-to-fine feature mining for video semantic segmentation. In *Proceedings of the IEEE/CVF Conference on Computer Vision and Pattern Recognition (CVPR)*, pages 3126–3137, 2022. **2**
- [36] Zachary Teed and Jia Deng. Deepv2d: Video to depth with differentiable structure from motion. In *International Conference on Learning Representations*, 2019. **2, 6, 7, 8, 15, 17**
- [37] Ashish Vaswani, Noam Shazeer, Niki Parmar, Jakob Uszkoreit, Llion Jones, Aidan N Gomez, Łukasz Kaiser, and Illia Polosukhin. Attention is all you need. In *Advances in neural information processing systems*, volume 30, 2017. **2, 4**
- [38] Chaoyang Wang, Simon Lucey, Federico Perazzi, and Oliver Wang. Web stereo video supervision for depth prediction from dynamic scenes. In *IEEE International Conference on 3D Vision (3DV)*, pages 348–357. IEEE, 2019. **2, 3, 5, 6, 7, 8, 15**
- [39] Qiang Wang, Shizhen Zheng, Qingsong Yan, Fei Deng, Kaiyong Zhao, and Xiaowen Chu. Irs: A large naturalistic indoor robotics stereo dataset to train deep models for disparity and surface normal estimation. In *IEEE International Conference on Multimedia and Expo (ICME)*, pages 1–6. IEEE Computer Society, 2021. **2, 5, 7, 8**
- [40] Wenshan Wang, Delong Zhu, Xiangwei Wang, Yaoyu Hu, Yuheng Qiu, Chen Wang, Yafei Hu, Ashish Kapoor, and Sebastian Scherer. Tartanair: A dataset to push the limits of visual slam. In *IEEE/RSJ International Conference on Intelligent Robots and Systems (IROS)*, pages 4909–4916. IEEE, 2020. **2, 5, 7, 8**
- [41] Yiran Wang, Zhiyu Pan, Xingyi Li, Zhiguo Cao, Ke Xian, and Jianming Zhang. Less is more: Consistent video depth estimation with masked frames modeling. In *Proceedings of the 30th ACM International Conference on Multimedia*, MM ’22, page 6347–6358, New York, NY, USA, 2022. Association for Computing Machinery. **2, 4, 6, 7, 15**
- [42] Ke Xian, Chunhua Shen, Zhiguo Cao, Hao Lu, Yang Xiao, Ruibo Li, and Zhenbo Luo. Monocular relative depth perception with web stereo data supervision. In *Proceedings of the IEEE/CVF Conference on Computer Vision and Pattern Recognition (CVPR)*, pages 311–320, 2018. **1, 11**
- [43] Ke Xian, Jianming Zhang, Oliver Wang, Long Mai, Zhe Lin, and Zhiguo Cao. Structure-guided ranking loss for single image depth prediction. In *Proceedings of the IEEE/CVF Conference on Computer Vision and Pattern Recognition (CVPR)*, pages 608–617, 2020. **1**
- [44] Enze Xie, Wenhui Wang, Zhiding Yu, Anima Anandkumar, Jose M Alvarez, and Ping Luo. Segformer: Simple and efficient design for semantic segmentation with transformers. *Advances in neural information processing systems*, 34:12077–12090, 2021. **3, 5, 11, 12**
- [45] Haofei Xu, Jing Zhang, Jianfei Cai, Hamid Rezaatofighi, and Dacheng Tao. Gmflow: Learning optical flow via global matching. In *Proceedings of the IEEE/CVF Conference on Computer Vision and Pattern Recognition (CVPR)*, pages 8121–8130, 2022. **4, 5, 11**
- [46] Weihao Yuan, Xiaodong Gu, Zuozhuo Dai, Siyu Zhu, and Ping Tan. Newcrfs: Neural window fully-connected crfs for monocular depth estimation. In *Proceedings of the IEEE/CVF Conference on Computer Vision and Pattern Recognition (CVPR)*, pages 3916–3925, 2022. **1, 2, 4, 8, 13**
- [47] Haokui Zhang, Chunhua Shen, Ying Li, Yuanzhouhan Cao, Yu Liu, and Youliang Yan. Exploiting temporal consistency for real-time video depth estimation. In *Proceedings of the IEEE/CVF International Conference on Computer Vision (ICCV)*, pages 1725–1734, 2019. **2, 6, 7, 15**
- [48] Xuaner Zhang, Kevin Matzen, Vivien Nguyen, Dillon Yao, You Zhang, and Ren Ng. Synthetic defocus and look-ahead autofocus for casual videography. *ACM Transactions on*

Graphics (TOG), 38(4), 2019. 1

- [49] Zhoutong Zhang, Forrester Cole, Richard Tucker, William T Freeman, and Tali Dekel. Consistent depth of moving objects in video. *ACM Transactions on Graphics (TOG)*, 40(4):1–12, 2021. 1, 2, 5, 6, 7, 8, 15, 17
- [50] Bolei Zhou, Hang Zhao, Xavier Puig, Sanja Fidler, Adela Barriuso, and Antonio Torralba. Scene parsing through ade20k dataset. In *Proceedings of the IEEE/CVF Conference on Computer Vision and Pattern Recognition (CVPR)*, pages 633–641, 2017. 5, 12

Appendix A. More details on the VDW Dataset

A.1. Dataset Construction

Data Acquisition and Pre-processing. Here we add more details on data acquisition and pre-processing (Sec. 4, line 466, main paper). Having obtained the raw videos, we use FFmpeg and PySceneDetect [28] to split all the videos into 104,582 sequences. We manually check and remove the duplicated, chaotic, and blur scenes. Videos that are wrongly split by the scene detect tools are also removed. Finally, we reserve 32,405 videos with more than six million frames for disparity annotation.

Disparity Annotation. In Sec. 4, line 474 of the main paper, we mentioned that the disparity ground truth is obtained via sky segmentation and optical flow estimation. Here we specify the details. Compared with common practice [30, 42], we introduce a few engineering improvements to make the disparity maps more accurate. As the sky is considered to be infinitely far, pixels in the sky regions should be segmented and set to the minimum value in the disparity maps. We find that using a single segmentation model [5, 20] like prior arts [30, 42] causes errors and noises in the sky regions. Hence, we generate the sky masks in a model ensemble manner. Each frame along with its horizontally flipped copy are fed into two state-of-the-art semantic segmentation models SegFormer [44] and Mask2Former [8], which yields four sky masks in total. A pixel is considered as the sky when it is positive in more than two predicted sky masks. Besides, we also fill the connected regions with less than 50 pixels to further remove the noisy holes in the sky masks. Such ensemble strategy can improve the quality of the ground truth as shown in Fig. A1, and consequently improves the performance of the trained models, especially on skylines as shown in Fig. A6 and A8.

Following the practice of previous single-image depth datasets [30, 42], we adopt a state-of-the-art optical flow model GMFlow [45] to generate the ground truth disparity of the left- and right-eye views. The estimated optical flow is bidirectional. We perform a consistency check between the optical flow pairs to obtain the valid masks for training. We adopt the adaptive consistency threshold for each pixel as [25]. The ground truth of each video is normalized by its minimum and maximum disparity. Then, the disparity value is discretized into 65,535 intervals. Fig. A4 shows more examples of our VDW dataset.

Invalid Sample Filtering. Having obtained the annotations, we further filter the videos that are not qualified for our dataset. According to optical flow and valid masks, samples with the following three conditions are removed: 1) more than 30% of pixels in the consistency masks are invalid; 2) more than 10% of pixels have vertical disparity larger than two pixels; 3) the average range of horizontal disparity is less than 15 pixels. Then, we manually check

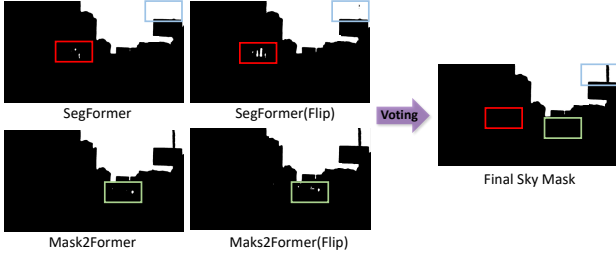


Figure A1: **Model ensemble strategy for sky segmentation on VDW dataset.** White area represents sky regions. Errors and noises in the rectangles are removed by model ensemble and voting, which improves the quality of the ground truth.

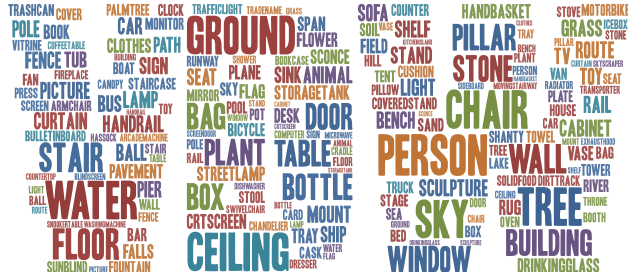


Figure A2: The word cloud of our VDW dataset.

all the videos along with their corresponding ground truth, and remove the samples with obvious errors. Finally, we retain 14,203 videos with 2,237,320 frames in VDW dataset.

A.2. Data Statistics

Here we add more statistics of VDW. Taking over 6 months to process, our VDW dataset contains 14,203 videos with 2,237,320 frames. The detailed data sources are listed in Table A1. Frame rates of all videos are over 24 fps. The minimum frame number is 18 while the maximum is 8,005.

To verify the diversity of objects in our videos. We conduct semantic segmentation with Mask2Former [8] trained on ADE20k [50]. All the 150 categories are covered in our dataset. The five categories that present most frequently are person (97.2%), wall (89.1%), floor (63.5%), ceiling (46.5%), and tree (42.3%). Each category can be found in at least 50 videos. Fig. A2 and Fig. A3 show the word cloud and detailed statistics of all the 150 categories.

Appendix B. More Details for NVDS

B.1. Decoder Architecture

Here we specify the decoder architecture. The decoder architecture is illustrated in Fig. A5. To fuse the depth-aware features from the backbone [44] and temporal features from the cross-attention module, feature fusion mod-

| Sources | Titles | Videos | Frames |
|---------------------------------|---------------------------------|--------|-----------|
| Documentaries | Deepsea Challenge | 210 | 38,078 |
| | Kingdom of Plants | 253 | 95,742 |
| | Little Monsters | 242 | 50,420 |
| | Jerusalem | 37 | 21,574 |
| Animations | Coco | 1,079 | 146,002 |
| | Kung Fu Panda 3 | 959 | 68,405 |
| Movies | Exodus: Gods and Kings | 1,339 | 99,146 |
| | Geostorm | 857 | 52,028 |
| | Hugo | 301 | 25,091 |
| | Mission: Impossible-Fallout | 664 | 46,344 |
| | Noah | 1,160 | 85,161 |
| | Pompeii | 158 | 10,112 |
| | Spider-Man: No Way Home | 914 | 75,077 |
| | The Legend of Tarzan | 735 | 64,840 |
| | The Three Musketeers | 253 | 18,180 |
| | Gravity | 191 | 38,332 |
| | Silent Hill 2 | 72 | 5,076 |
| | Transformers: Age of Extinction | 1,323 | 84,619 |
| | Doctor Strange | 299 | 23,779 |
| Battle of the Year | 454 | 19,613 | |
| Justice League | 428 | 37,202 | |
| The Hobbit 2 | 644 | 53,391 | |
| The Great Gatsby | 729 | 49,079 | |
| Billy Lynn's Long Halftime Walk | 242 | 29,137 | |
| Web Videos | YouTube | 660 | 58,140 |
| All | - | 14,203 | 2,237,320 |

Table A1: **Video and frame numbers statistics of the four data sources.** Our VDW dataset contains 14,203 videos from movies, animations, documentaries, and web videos.

ules (FFM) [20, 21] and skip connections are adopted. Resolutions are gradually increased while channel numbers are decreased. At last, we use an adaptive output module to adjust the channel and restore the disparity maps.

B.2. Loss Function

As mentioned in Sec. 3.3, line 352 in the main paper, the training loss consists of a spatial loss and a temporal loss. Here we specify the computation process.

For the spatial loss, we adopt the widely-used affinity invariant loss and gradient matching loss [29, 30] as \mathcal{L}_s . For the affinity invariant loss, let D and D^* denote the predicted disparity and ground truth respectively, we first calculate the scale and shift:

$$t(D) = \text{median}(D), s(D) = \frac{1}{M} \sum_{i=1}^M |D_i - t(D_i)|, \quad (9)$$

where M denotes the number of valid pixels. The prediction and the ground truth are aligned to zero translation and unit scale as follows:

$$\tilde{D} = \frac{D - t(D)}{s(D)}, \tilde{D}^* = \frac{D^* - t(D^*)}{s(D^*)}. \quad (10)$$

Then the affinity invariant loss can be formulated as:

$$\mathcal{L}_{af} = \frac{1}{M} \sum_{i=1}^M |\tilde{D} - \tilde{D}^*|. \quad (11)$$

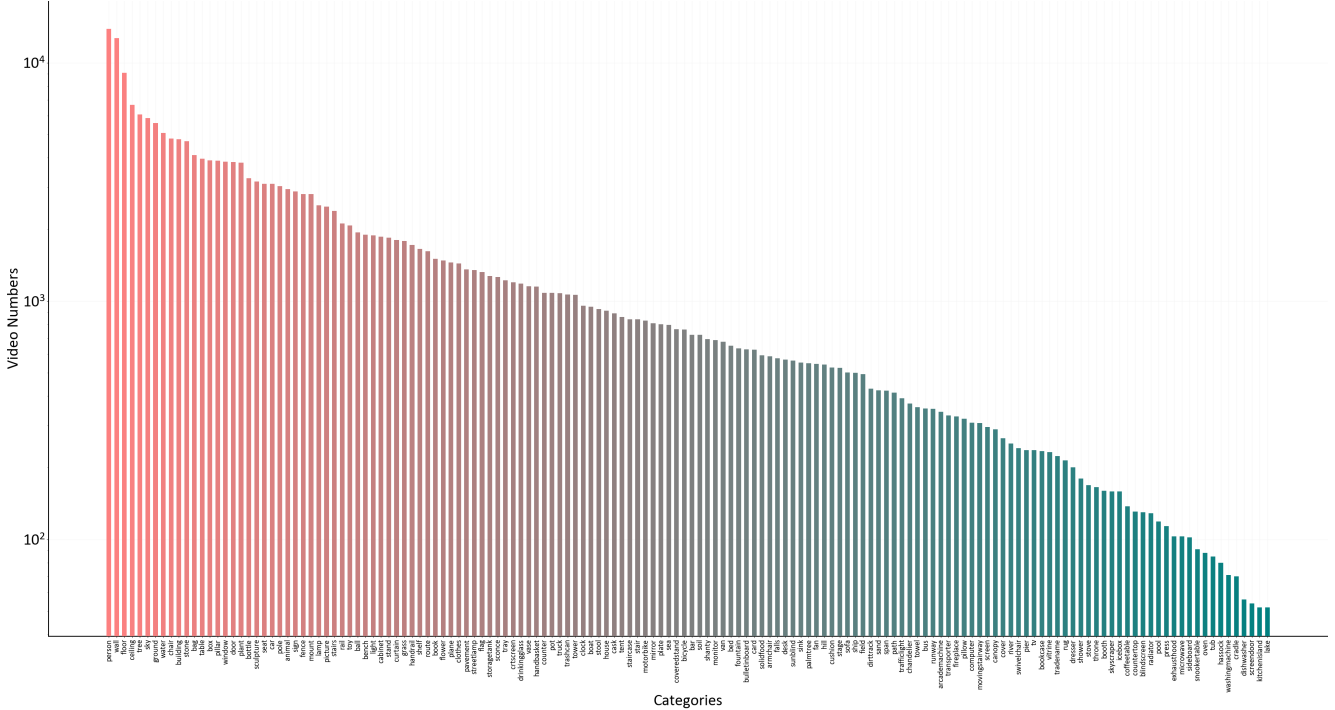


Figure A3: The statistics of the 150 semantic categories in VDW dataset.

Besides, we also adopt the multi-scale gradient matching loss [30], which can improve smoothness of homogeneous regions and sharpness of discontinuities in the disparity maps. The gradient matching loss is formulated as:

$$\mathcal{L}_{grad} = \frac{1}{M} \sum_{k=1}^K \sum_{i=1}^M (|\nabla_x R_i^k| + |\nabla_y R_i^k|), \quad (12)$$

where $R_i = \tilde{D}_i - \tilde{D}_i^*$, and R^k denotes the difference between the disparity maps at scale $k = 1, 2, 3, \dots, K$ (the resolution is halved at each level). Following [29], we set $K = 4$ and set the weight β of \mathcal{L}_{grad} to 0.5. The spatial loss can be expressed as:

$$\mathcal{L}_s = \mathcal{L}_{af} + \beta \mathcal{L}_{grad}, \quad (13)$$

Temporal loss. In line 362 of the main paper, we mentioned that the temporal loss is masked with a visibility mask $O_{n \Rightarrow n-1}$ calculated from the warping discrepancy between frame F_n and the warped frame \hat{F}_{n-1} . This mask is obtained by:

$$O_{n \Rightarrow n-1} = \exp(-\gamma \|F_n - \hat{F}_{n-1}\|_2^2). \quad (14)$$

We set $\gamma = 50$ and use bilinear sampling layer for warping.

Appendix C. More Experimental Results

C.1. Depth Metrics

Here we specify the evaluation metrics for depth accuracy. we adopt commonly-applied depth evaluation metrics: Mean relative error (Rel) and accuracy with threshold t .

Mean relative error (Rel): $\frac{1}{M} \sum_{i=1}^M \frac{\|D_i - D_i^*\|_1}{D_i^*}$;

Accuracy with threshold t : Percentage of D_i such that $\max(\frac{D_i}{D_i^*}, \frac{D_i^*}{D_i}) = \delta < t \in [1.25, 1.25^2, 1.25^3]$, where M denotes pixel numbers, D_i and D_i^* are prediction and ground truth of pixel i .

C.2. Model Efficiency

Here we evaluate the efficiency of the proposed Neural Video Depth Stabilizer (NVDS) in detail. Model parameters and FLOPs are reported in Table A2. The FLOPs are evaluated on a 384×384 video with four frames. The stabilization network of NVDS only introduces limited computation overhead compared with the off-the-shelf depth predictors.

| | DPT-L [29] | NeWCRFs [46] | Midas-v2 [30] | Stabilization Network |
|----------------|------------|--------------|---------------|-----------------------|
| FLOPs (G) | 1011.32 | 550.47 | 415.24 | 254.53 |
| Params (M) | 341.26 | 270.33 | 104.18 | 88.31 |

Table A2: Comparisons of FLOPs and model parameters.



Figure A4: More examples of our VDW dataset. Sky regions and invalid pixels are masked out.

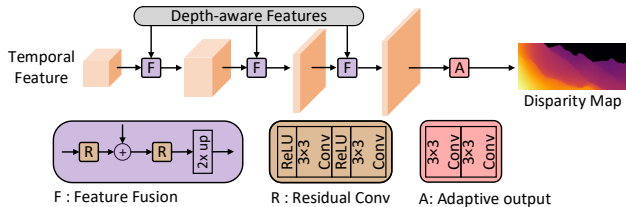


Figure A5: The architecture of decoder.

| Method | $\delta_1 \uparrow$ | $\delta_2 \uparrow$ | $\delta_3 \uparrow$ | $Rel \downarrow$ | $OPW \downarrow$ |
|-----------------|---------------------|---------------------|---------------------|------------------|------------------|
| Midas [30] | 0.644 | 0.853 | 0.928 | 0.347 | 0.647 |
| DPT [29] | <u>0.724</u> | <u>0.890</u> | <u>0.950</u> | <u>0.266</u> | 0.461 |
| ST-CLSTM [47] | 0.461 | 0.708 | 0.836 | 0.589 | 0.455 |
| FMNet [41] | 0.465 | 0.712 | 0.837 | 0.584 | 0.388 |
| DeepV2D [36] | 0.522 | 0.728 | 0.833 | 0.628 | 0.425 |
| WSVD [38] | 0.621 | 0.825 | 0.912 | 0.379 | 0.437 |
| Robust-CVD [16] | 0.658 | 0.855 | 0.928 | 0.334 | 0.251 |
| Ours(Midas) | 0.694 | 0.879 | 0.943 | 0.286 | <u>0.164</u> |
| Ours(DPT) | 0.731 | 0.895 | 0.952 | 0.259 | 0.138 |

Table A3: **Comparisons on VDW dataset.** The first 2 rows show the results of different single-image depth predictors. The next 5 rows contain video depth approaches. The last 2 rows consist of the results of our NVDS. Best performance is in boldface. Second best is underlined.

| Method | $\delta_1 \uparrow$ | $\delta_2 \uparrow$ | $\delta_3 \uparrow$ | $Rel \downarrow$ | $OPW \downarrow$ |
|--------------------------|---------------------|---------------------|---------------------|------------------|------------------|
| Midas [30] | 0.485 | 0.693 | 0.787 | 0.410 | 0.843 |
| DPT [29] | 0.597 | <u>0.768</u> | <u>0.846</u> | <u>0.339</u> | 0.612 |
| ST-CLSTM [47] | 0.351 | 0.571 | 0.706 | 0.517 | 0.585 |
| FMNet [41] | 0.357 | 0.579 | 0.712 | 0.513 | 0.521 |
| DeepV2D [36] | 0.486 | 0.674 | 0.760 | 0.526 | 0.534 |
| WSVD [38] | 0.501 | 0.709 | 0.804 | 0.439 | 0.577 |
| CVD [24] | 0.518 | 0.741 | 0.832 | 0.406 | 0.497 |
| Robust-CVD [16] | 0.521 | 0.727 | 0.833 | 0.422 | 0.475 |
| Zhang <i>et al.</i> [49] | 0.522 | 0.727 | 0.831 | 0.342 | 0.481 |
| Ours(Midas) | 0.532 | 0.731 | 0.833 | 0.374 | <u>0.469</u> |
| Ours(DPT) | <u>0.591</u> | 0.770 | 0.849 | 0.335 | 0.424 |

Table A4: **Comparisons on the Sintel dataset.** We only report CVD [24] and Zhang *et al.* [49] on the 12 videos with valid outputs, while other methods are on the 23 videos.

C.3. More Quantitative Comparisons

In the main paper, only δ_1 , Rel , and OPW are reported. The additional results on the VDW and the Sintel [6] dataset are shown in Table A3 and Table A4. Besides, as CVD [24] and Zhang *et al.* [49] cannot produce results on 11 of 23 videos in Sintel [6] dataset, we additionally report the results on the other 12 videos in Table A5.

| Method | $\delta_1 \uparrow$ | $\delta_2 \uparrow$ | $\delta_3 \uparrow$ | $Rel \downarrow$ | $OPW \downarrow$ |
|--------------------------|---------------------|---------------------|---------------------|------------------|------------------|
| Midas [30] | 0.670 | 0.853 | 0.902 | 0.246 | 0.712 |
| DPT [29] | 0.747 | 0.874 | 0.917 | 0.196 | 0.671 |
| ST-CLSTM [47] | 0.477 | 0.711 | 0.827 | 0.366 | 0.547 |
| FMNet [41] | 0.492 | 0.728 | 0.825 | 0.363 | 0.516 |
| DeepV2D [36] | 0.509 | 0.735 | 0.827 | 0.384 | 0.575 |
| CVD [24] | 0.518 | 0.741 | 0.832 | 0.406 | 0.497 |
| Zhang <i>et al.</i> [49] | 0.522 | 0.727 | 0.831 | 0.342 | 0.481 |
| WSVD [38] | 0.621 | 0.822 | 0.891 | 0.305 | 0.581 |
| Robust-CVD [16] | 0.673 | 0.848 | 0.888 | 0.284 | 0.447 |
| Ours(Midas) | 0.700 | 0.866 | 0.918 | 0.226 | <u>0.425</u> |
| Ours(DPT) | <u>0.741</u> | 0.876 | 0.926 | <u>0.205</u> | 0.411 |

Table A5: **Comparisons on the 12 videos of Sintel [6] dataset.** We test the 12 videos that CVD [24] and Zhang *et al.* [49] can produce results for fair comparisons.

C.4. More Qualitative Results.

We show more visual comparisons in Fig. A6, A7, A8 and A9. Please refer to the supplementary video for video depth visualization results. We draw the scanline slice over time. Fewer zigzagging pattern means better consistency. We also elaborate video demos and visualizations. Please refer to our project page: <https://github.com/RaymondWang987/NVDS>.

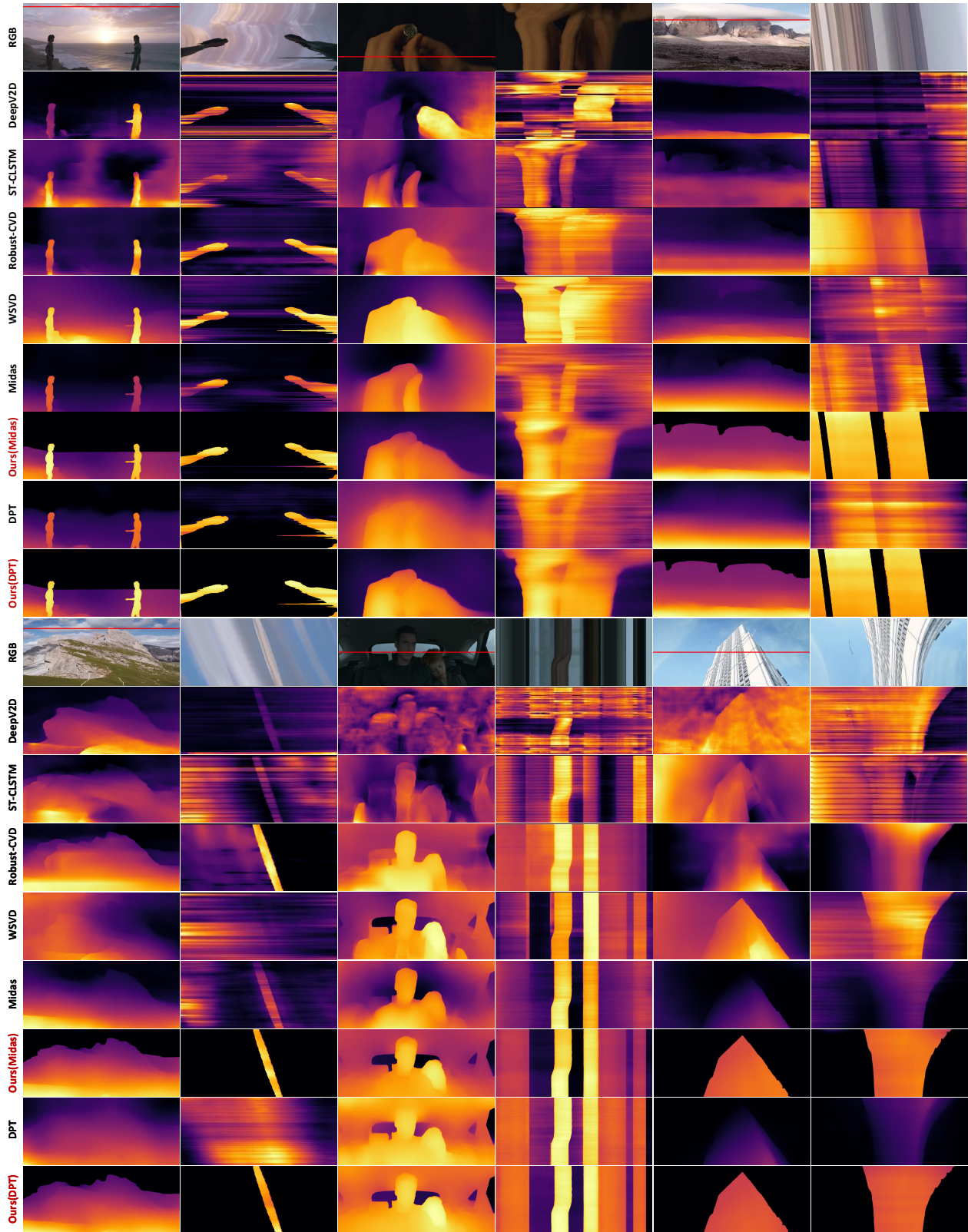


Figure A6: **More qualitative results on natural scenes.** The first image in each pair is the RGB frame, while the second is the scanline slice over time. Fewer zigzagging pattern means better consistency.

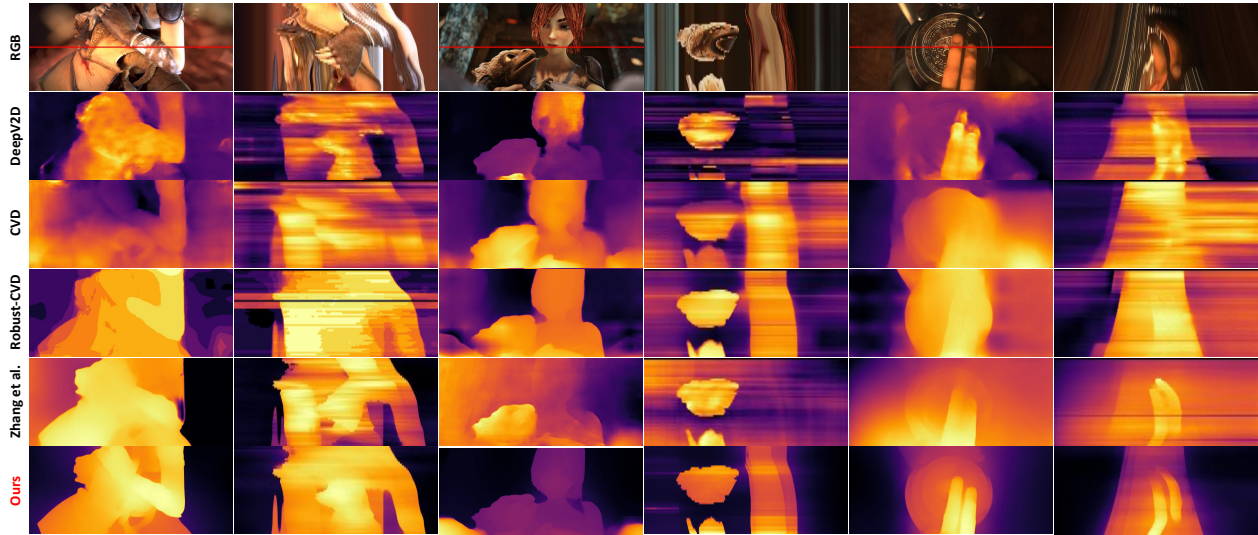


Figure A7: **Qualitative results on Sintel [6] dataset.** We compare the results of DeepV2D [36], CVD [24], Robust-CVD [16], and Zhang *et al.* [49]. Without relying on test-time training [16, 24, 49], we conduct zero-shot evaluations on Sintel [6] and achieve significantly better performance than those TTT-based methods [16, 24, 49].

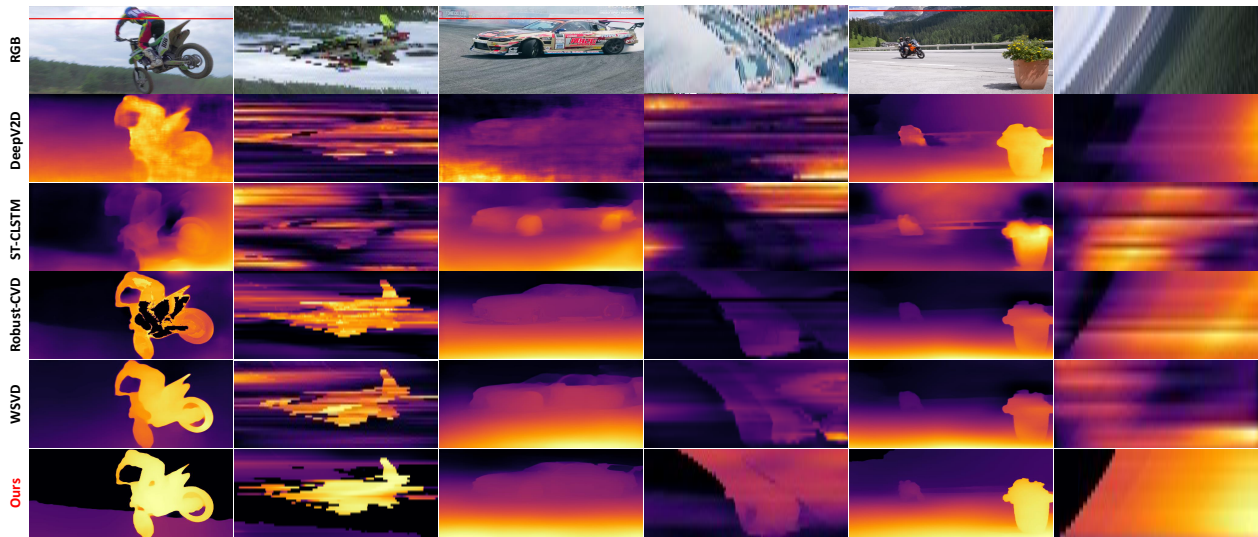


Figure A8: **Qualitative results on DAVIS [27] dataset.** We achieve better performance than prior arts on natural scenes.

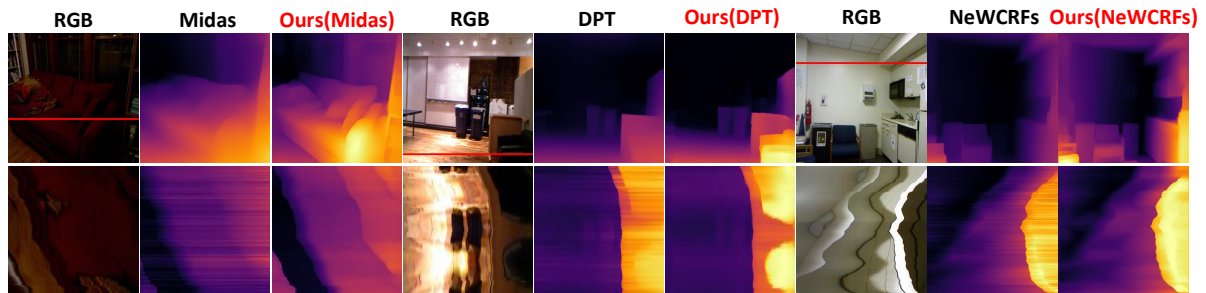


Figure A9: **Qualitative results on NYUDV2 [33] dataset.** We compare three different single-image depth predictors.